Turbulence and flow field alterations inside a fish sea cage and its wake

Pascal Klebert*, Biao Su

Sintef OCEAN, Seafood Technology, Aquaculture Structures, Postboks 4762, Torgarden, Trondheim 7465, Norway

ABSTRACT

Measurements were performed inside and in the wake of a commercial salmon sea cage. The key instrumentation included the following: sea bottom-mounted acoustic Doppler current profilers providing continuous concurrent flow velocity and turbulence information about the water columns; vessel-mounted acoustic current profilers mapping the flow pattern around the wake of the cage in a selected incoming flow; a microstructure profiler measuring the fluctuations in vertical shear in the dissipation range; an acoustic Doppler velocimeter measuring the velocity inside the sea cage; dissolved oxygen sensors and echosounders measuring the distribution of fish inside the cage. The measurements have performed with stocked and emptied sea-cage. The results showed simultaneous strong flow reductions in the wake near the cage and high turbulence in the upper part of the water column, both of which were generated by the sea cage. Measurements inside the cage showed that although the schooling fish reduced the flow, there was no evidence that they generate secondary radial and vertical flows.

1. Introduction

Because of the increasing demand for seafood worldwide and the limitations of captured fishery production, aquaculture has become a fast-growing and significant source of food. According to the Food and Agriculture Organization (FAO) (2018) [1], in 2016, aquaculture production increased by four million tons over the previous year, and it was predicted that in 2030, 109 million tons would be produced, a growth rate of 37% over 2016. The sustainability of sea-cage farming, which is an important part of this production, has improved greatly in the past year.

The current flow patterns around and within fish farms are extremely complex (Klebert et al. [2, 3]). The fluid-structure interaction for the net cage is gaining increasingly more attention and research efforts: Bi et al. [4] investigated waves propagating through net cages with different levels of biofouling and studied them numerically using a three-dimensional computational fluid dynamics model. Kim et al. [5] used also computational fluid dynamic software to analyze the flow field characteristics of a submersible aquaculture cage, Zhao et al. [6] performed an experimental study on flow velocity and mooring loads for multiple net cages in steady current. But laboratory measurements alone cannot be used to predict their hydrodynamics because of the variable topology on site (Rasmussen et al. [7]), which generates a complex flow structure. The flow regime inside a cage depends on the incoming current (Klebert et al. [8]; Gansel et al. [9].) as well as the effects of the fish and their behavior (Johansson et al. [10]). The physical factors that modify hydrodynamic flows within farms include water depth (Klebert et al. [3]), current flow velocity, and water stratification (i.e., salinity and temperature). In addition, recent studies (Klebert and Arneborg [11]; Plew et al. [12]) showed that the microturbulence created by salmon swimming in both tanks and net-pen cages generated eddies that varied from approximately one fish-body length down to only a few millimeters. Klebert and Arneborg [11] measured the occurrence of micro-scale turbulence caused by swimming salmon, which spread for a distance of four to five cage diameters in the wake of a cage. In addition, a significant reduction in current flow was observed (Klebert et al. [2]). These complex interactions (i.e., current flows in fish farms) have a significant effect on the distribution of particulate matter surrounding fish farms. For example, turbulence keeps some particles suspended, and flow reduction simultaneously causes the sedimentation of other particles near the cages. The combination of these factors greatly affects the distribution of waste feed and salmon feces both horizontally and vertically near the internal and peripheral areas of farms by influencing their dispersal. Furthermore, farming systems that use skirts in the upper part of the cages as a preventive measure against lice infestation increase the complexity of flows compared to conventional net cage systems, which requires investigation. These effects are strongly enhanced in a fish farm with a high density of fish and complex flow patterns, which are caused by the layout of the farm, such as single rows, grid systems, or an orientation against the flow direction.
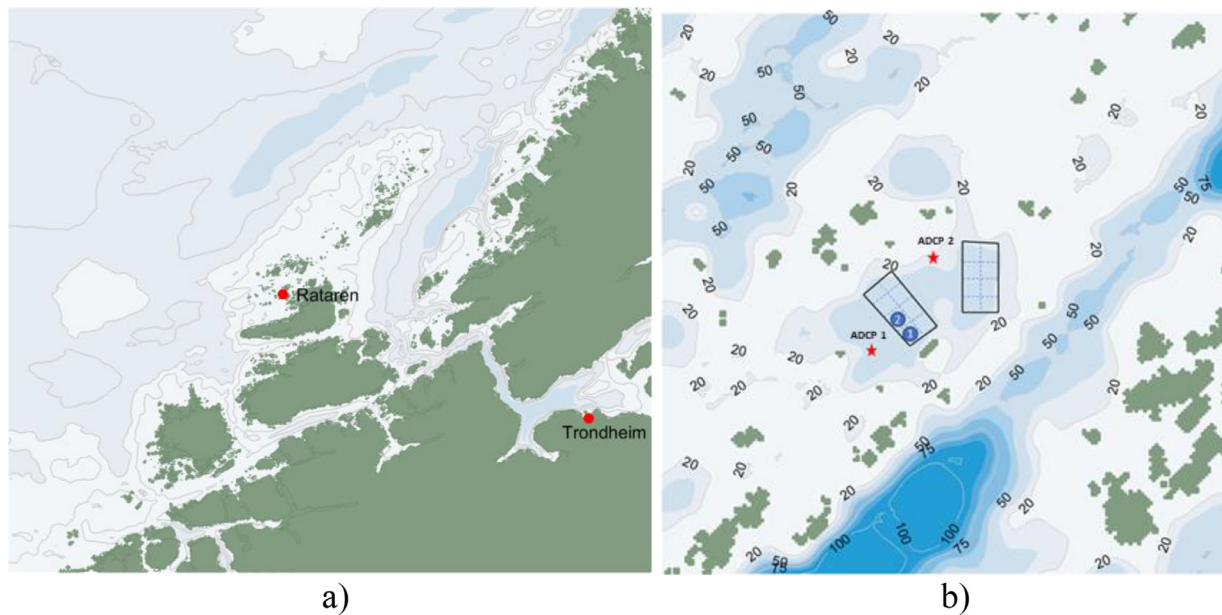
---

* Corresponding author.
 E-mail address: pascal.klebert@sintef.no (P. Klebert).

Fig. 1. (a) Measurement site, Rataren at 63˚46.966 N, 8˚31.364E; (b) farm layout: only two cages were on site at the time of the measurement (locations of the bottom-mounted ADCPs are indicated with red stars (63˚46.723 N, 8˚30.883 E and 63˚46.949 N, 8˚31.260 E). (For interpretation of the references to color in this figure legend, the reader is referred to the web version of this article.)

2. Materials & methods

2.1. Site description

The fish farm used in this study is located in Rataren (63˚46.966 N, 8˚31.364E), a commercial marine salmon production facility located in the north of the island of Frøya in Middle Norway. This is a relatively exposed location in a coastal environment. The region is influenced by two major current systems: the Norwegian Coastal Current (NCC) (Skagseth et al. [13]) and the Norwegian Atlantic Current (NAC) (Sætre [14]). Fig. 1 shows the location of the farm on the Norwegian coast. At the time the measurements were taken, in August 2018, only two cages (1 & 2) were used for production in August 2018 during phase A and in October 2018, as the fish were harvested, the same cages, but emptied, were used during phase B. The net cages were the standard type used in Norway. These conic-shaped bottom nets were 50 m in diameter, 15 m in depth for the circular vertical part, and 12 m in depth for the cone net at the bottom. The cages were surrounded by an impermeable skirt from the sea surface to a depth of 10 m to shield the upper part of the cage from sea lice infestation (Frank et al. [15].).

The bathymetry data were provided by the Norwegian Mapping Authority (www.kartverket.no). Beneath the fish farm cages, the bottom sloped from about a plateau of 30 m to about 45 m under the farm, which corresponded to a 8-degree slope (distance between the cage and the plateau is around 100 m). The measurements were carried out inside and in the immediate vicinity of cage 2 as well as, in a limited area around the farm (Fig. 1 and Fig. 11).

2.2. Equipment description

Several sensors were used to measure tidal currents and elevations, micro-scale turbulence, vertical temperature profiles, velocity inside the cage, vertical fish distribution in the cage, and the dissolved oxygen (DO) level inside and outside the cage. The measurements were performed during the two periods: cage 2 with fish (Phase A: 2018.08.7–16) and cage 2 without fish (Phase B: 2018.10.09–11). During the measurement in phase A, cage 2 held approximately 120,000 salmon at an average weight of 5.5 kg.

2.2.1. Bottom-mounted and moving current profilers (ADCP)

Teledyne RDI Sentinel V50 500 (kHz) current profilers were used to measure the current flow. All ADCPs (Acoustic Doppler Current Profiler) were configured as 0.5 m bin cell size and a sampling rate of 2 Hz. The instruments had four beams slanted at 25˚ from the vertical in addition to a fifth vertical beam. The standard deviation in the measurements associated with this setup was 0.6 cm/s. These ADCPs were used in two different ways: a) mounted facing upward on Oceanscience Sea Spider tripods with a gimbal and deployed on the sea bottom, which provided data with limited spatial resolution; b) mounted facing downward on a moving Automated Surface Vehicle (ASV), which provided large spatial resolution. In the latter, the ASV was nonmagnetic, and the small propellers used for propulsion were plastic, so no alteration in the compass was expected. The bottom tracking (BT) feature integrated in the sensor was used (a) to calibrate the ADCP prior to each transect to ensure that the measured currents magnitude and direction must be independent of the ASV direction and (b) during the measurements as a reference for both water velocity and boat speed. The average ASV speed was less than 0.3 m/s. The courses of the ASV were programmed prior to each measurement to cover an area of the wake at cage 2. Several transects at equal distance intervals were collected within a short period to capture realistic current flow patterns in a large spatial resolution. The depth of the transducer head was 0.3 m below the sea surface and the cell size was 1 m height. The measurement positions were logged using the Vector V104 GPS Smart Antenna (Hemisphere GNSS), which provides differential GPS positions in order to achieve accurate heading and position performance. The GPS coordinates were acquired sequentially using the ADCP measurements. The commercial software VMDAS (Teledyne) was used to collect the data, and WINADCP was used to visualize and partly post-process the data. The ADCP was directly linked to a laptop to view the flow measurement instantaneously. Similar measures were used by Rasmussen et al. [7], but in the present study, the automated GPS-based procedure of the ASV insured that a proper grid map would be formed by the measurements area downstream and upstream of the cage. Data interpolation was carried out using the MATLAB® (The Math Works Inc., Natick MA, USA) scripts developed based on previously published methods (Hajovsky et al. [22]).

Table 1
Overview of the different periods used to plot the velocity fields and echo-sounder signals inside the cage.

Phase	Date	Time interval	Flow direction	Cage
A.1	08.15.2018	03:00–07:00	NE → SW	Stocked
B.1	10.11.2018	02:00–06:00	NE → SW	Emptied
A.2	08.15.2018	10:00–14:00	SW → NE	Stocked
B.2	10.11.2018	08:00–12:00	SW → NE	Emptied
A.3	08.15.2018	16:00–20:00	NE → SW	Stocked
B.3	10.11.2018	14:00–18:00	NE → SW	Emptied
A.4	08.15.2018	22:00–02:00	SW → NE	Stocked
B.4	1011.2018	20:00–00:00	SW → NE	Emptied

2.2.2. Turbulence profiler

The micro-scale turbulence was measured using a 1-m loose-tethered, free-fall Rockland Scientific International (RSI) vertical micro-structure profiler (MicroCTD). This sensor is used to measure vertical profiles of temperatures, conductivity, and centimeter-scale vertical gradients of temperature and conductivity. It is equipped with two shear probes and a FP07 thermistor. All fast probes were sampled at 512 Hz. The profiler was also equipped with conductivity, temperature, and pressure at a sampling frequency of 64 Hz (JFE Advantech).

The microstructure measurements were carried out at 512 Hz and stored at 64 Hz; the CT sensor was operated at 16 Hz. The profiles were performed in two ways using a 13 m twin-hulled boat: after a clearly established flood or ebb regime, the turbulence profiles were recorded (a) while the boat was freely drifting in front and downstream of the cage and (b) in a static location at the leeward side of the cage. The typical profiling speeds were between 0.75 and 0.8 m/s during each profile. When the sensor approached the bottom, the tether was pulled taut and the profiler was reeled back to the surface and then released to measure another vertical profile. In the present study, the shear measurements from the MicroCTD were used to estimate the dissipation rates of turbulent kinetic energy (TKE). Every profile provided two shear measurements. The dissipation rate (ε) was calculated using the software provided by Rockland Scientific. The obtained data above 3 m water depth was excluded from the analysis considering possible disturbances by the boat (the draft of the boat was 1 m) and excessive inclination of the falling MicroCTD; the dissipation of TKE was analyzed following the method described by Wolk et al. [16]. and revised by Lueck [17].

2.2.3. ADV current meters

Inside cage 2, the three components of current velocity were measured using a Nortek Vector Acoustic Doppler Velocimetry (ADV) that was hung from the surface by a buoy and maintained in a vertical orientation with a bottom load. The sampling rate was 4 Hz: 120 samples per burst and the burst interval was 60 s. The sensors were located in the center of the cage and 18 m from the center, at two different depths: 1.5 m and 12 m.

2.2.4. Echosounders

Two single-beam scientific echosounders (SIMRAD EK15 200 kHz) were used to monitor the vertical distribution of the fish in the cage at two different locations: in the center of the cage and 18 m from this center. The measurements were taken from the surface, and care was taken that the measurement signal was not affected by the ADV sensors located at similar distances from the center.

2.2.5. DO sensors

Six dissolved oxygen (DO) sensors (MiniDOT, PME, Vista, CA, USA) were located at three different depths inside the cage (1 m, 5 m, and 11 m) along the same rope that was used to hang the ADVs. Three other sensors at the same depths were located 400 m outside the cage and measuring reference values. All sensors were sampled at 1 min intervals.

3. Results and discussion

3.1. Measurement data inside the cage: echosounders, do oxygen, and velocity

The velocity data collected from the Nortek vectors were filtered using a phase space filter (Goring and Nikora [18]) to remove velocity spikes due to not only Doppler noise, signal aliasing, or other instrument noises but also spikes caused by fish either in the sample volume or swimming through one or more of the acoustic beams. The mean values of velocity were calculated using the velocity data from which the spikes were removed (no replacement). No velocity spectra were calculated from these data, as the sensors did not hang in a completely motionless way. The results of the measurements during the two phases (A and B (Table 1)) were compared with the aim of segregating the possible effects of the schooling fish on the internal flow of the cage. For that purpose, different periods with clear incoming flow magnitude and direction were selected for the two phases and then plotted separately (A.x: Measurements with fish (Phase A); B.x: Measurements with empty cage (Phase B)). The results are represented in Fig. 3, Fig. 4, Fig. 5, Fig. 6 as follows: each phase is divided into two main parts: on the left are the velocity rose magnitude and direction (V11: Horizontal and vertical components) and the corresponding echosounder (TR1) signal located 18 m from the center of the cage. On the right side, the same type of data are plotted (i.e., two velocity signals from the two velocity sensors located at two different depths (V21:2 m and V22:12 m) and the echosounder (TR2) (see Fig. 2 for the location of these sensors) located in the center of the cage.

The incoming flow direction was measured by the velocity sensor located in the center of the cage at 12 m from the surface and so under the skirt. Four flow directions were plotted (Table 1): two toward the north and two toward the south at different times of the day and with or without fish. The main difference between the cases with (Phase A) and without fish (Phase B) was that the velocity field in the upper part of the cage and shielded by the skirt was more scattered in Phase A because
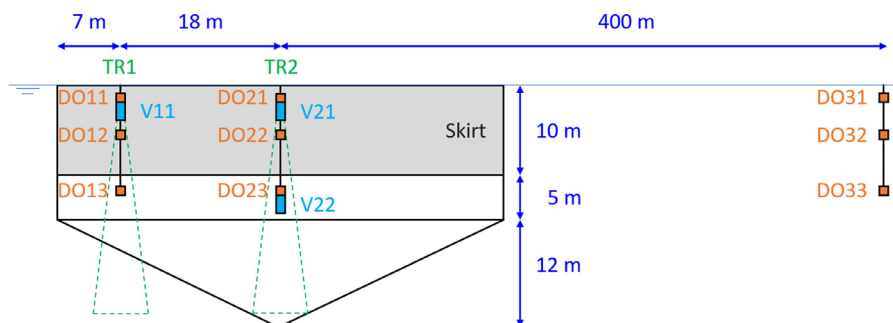
Fig. 2. Measurement area and sensor location. Echosounders (TR), ADVs (V), and oxygen sensors (DO).
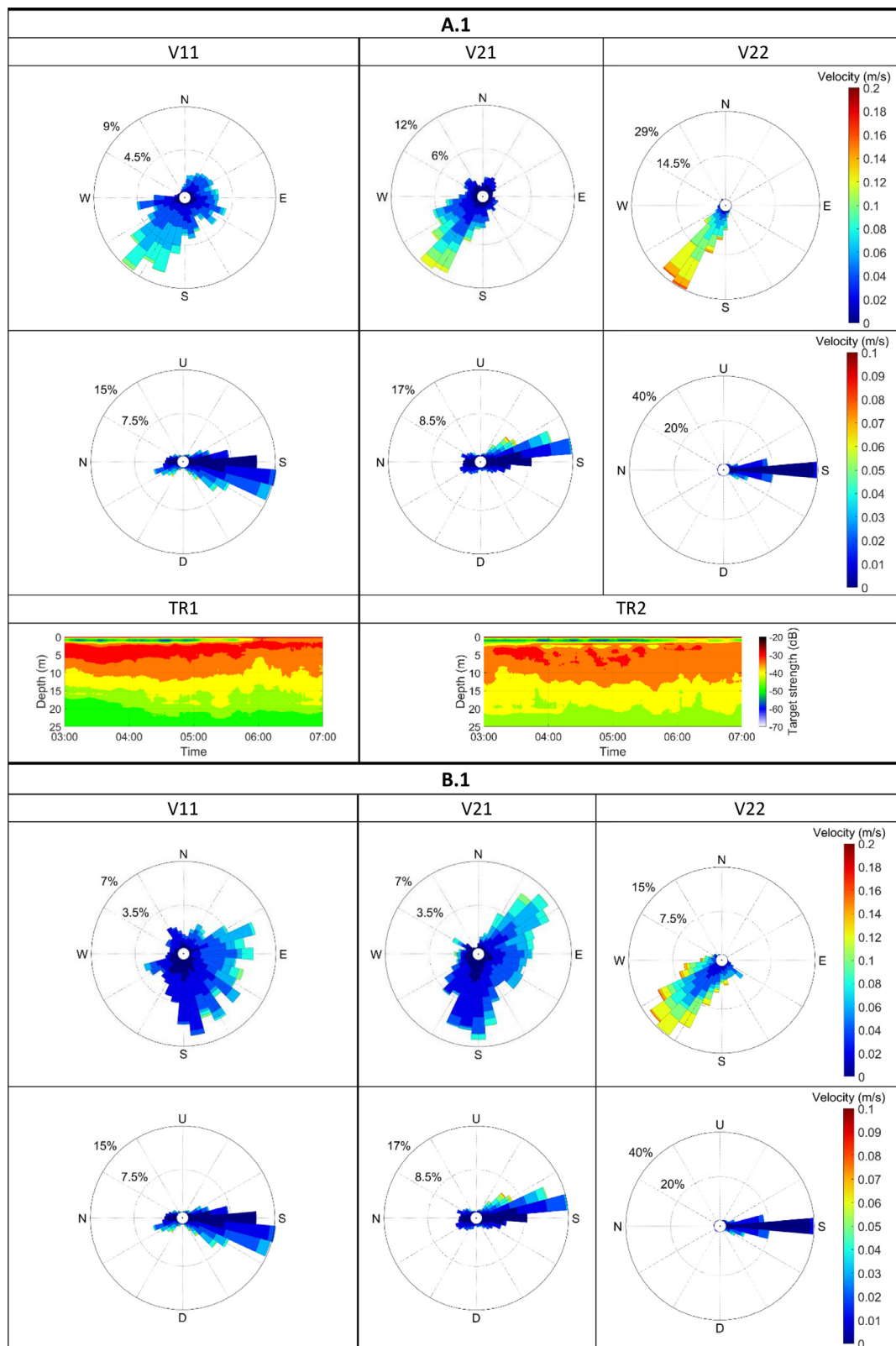
Fig. 3. Velocity magnitude (Horizontal vertical components (represented only for A.1 and B1) and current rose, of the velocity inside the cage at different depths and locations (V11, V21, V22). In Phase A (with stocked cage), the corresponding signals of the echosounders at the same locations are added.

the fish were circling around the cage. The vertical components of the velocity field inside the volume shielded by the skirt was not completely negligible in both Phase A and Phase B, which made difficult to speculate the exact contribution of the schooling fish to this pattern. The

measured vertical component in the case of the empty cage (Phase B) was probably linked to the flow moving under the shirt, which was caused by its deformation (Lien et al. [19]).

ADV V22, is being located below the skirt, so gives also the

incoming flow direction with some flow reduction.

- For an incoming flow direction SW→NE, B.2 and B.4 show that the ADV V21 in the upper middle part, measured an opposite flow direction, meaning that the water inside of the skirt travels in opposite direction of the undisturbed current as shown by Lien et al. [19] with flow simulations with emptied cage. In the corresponding cases with stocked cage A.2 and A.4, this recirculation can be barely seen most probably due to the fish distribution especially for A.4 during which most fish gathered at the surface at night.
- For an incoming flow direction NE→SW, the stocked cage in A1 and A3 do not show any recirculation in the shielded volume but in contrary a flow direction similar to the incoming flow. The emptied cages B1 and B3, do not show neither any recirculation and unlike B.2 and B.4, exhibit a flow with scattered direction inside the shielded volume. This difference is most probably due to a lower incoming flow velocity.

The temperatures measured by the MiniDOT sensor were almost constant at all three depths (1, 5, 11 m) at around 12–13 °C ($\pm$ 0.5 °C) with the maximum occurring in the middle of the day during Phase A (not presented here). A more precise overview of the temperature gradient profiles with depth is provided by the MicroCTD (see Section 3.2.2). The salinity measured by the MicroCTD was about 33.5 PSU during Phase A and 32.5 PSU during Phase B.

Fig. 4 shows the DO variations at different depths and locations inside the cage as well as the echosounder signals. As shown in Fig. 4, the DO level measured at the reference location (black line) indicated an average value of 8.3 mg/l in the three depths (1m–5 m–11 m). Inside the cage, the oxygen conditions were directly related to the vertical distributions of the fish. The fish were fed almost all the time in daylight during the study, which was a multiple behavioral trade-off between surface light avoidance, surface feeding, and feeding motivation during the day and gathering close to the surface during the night (Oppedal et al. [20]). The lowest oxygen level at the surface was measured in the middle of the night because of the high concentration of fish in the upper part of the shielded volume. Insufficient oxygen supply (environmental hypoxia) is primarily considered a problem during the summer and the autumn, occurring in short frequent periods rather than prolonged periods. However, in this study, no hypoxia tolerance threshold (50% O_2) (Solstorm et al. [21]) was measured, including during the period corresponding to the turn of tidal currents. The recorded DO in the cage ranged from 58 to 95% saturation with high degrees of vertical, horizontal, and temporal variations. The poorest DO conditions occurred consistently at night in the volume shielded by the skirt, where most of the fish gathered in the first few meters under the surface.

3.2. Data on flow pattern outside the cage

3.2.1. Static adcp

During the two phases, static ADCPs were mounted on a tripod with gimbals and deployed on the sea bottom and set to record the beam velocities at a ping rate of 2 Hz. The temporal variations in the magnitude and direction of the current flow at different depths was recorded by ADCP 1 during the two phases (Fig. 8).

3.2.2. Moving adcp

From the raw data acquired by the ADCP, 10 s average data were generated and used in the processing with the maximum velocity of the ASV (0.3 m/s), which allowed an ensemble space of about 2 m (Fig. 9). The horizontal velocity fields were estimated from these vertical transects by using a triangulation-based natural neighbor interpolation in MATLAB with the "griddata" function. This function fits the surface of the form $z = f(x,y)$ to the data in the non-uniformly spaced vectors (x, y, and z). It interpolates this surface at the points specified by (Xi and

Yi) to produce Zi and defines the type of surface fit to the data, producing smooth surfaces that always pass through the data points and forming a uniform grid (Hajovsky et al. [22]). The first vertical profile is located at 60 m behind cage2 and the interval distance between each vertical profile is 30 m, so the last profile is at 150 m (3 times the cage diameter) behind cage2 where flow reduction from the cage is still monitored.

Løland [23] proposed a theoretical expression for the non-dimensional velocity u_w/U_0 (r) behind a net panel based on the solidity of the nets ($S_n = 0.22$, in these measurements). It is based on a source-model and is uniform throughout the entire wake.

$$\frac{u_w}{U_0} = r = 1 - 0.46C_d \tag{1}$$

where u_w is the flow velocity in the wake of the cage and U_0 is the free-stream velocity. C_d is calculated from S_n with the following expression

$$C_d = 0.04 + (-0.04 + 0.33S_n + 6.54S_n^2 - 4.88S_n^3) \tag{2}$$

which gives $u_w/U_0 = 0.84$ for one net panel, and $u_w/U_0 = 0, 71$ for two net panels which will represent the flow reduction through a cage.

An example of the velocity reduction behind the net cage is given in the table 2, by using the velocity behind the cage in the first transect (60 m distance). As expected, the skirt around the cage reduced more the flow in the first 10 m in the water column than the netting below. A reasonable comparison with Løland reduction factor (r) can be seen for a depth 14 m but for 12 m, a higher reduction is measured: the latest could be due from different factors like most probably to the flow interaction with the bottom of the skirt, or the hang ratio of the net mesh which affect real solidity of the netting (Zhao et al. [24]), the attack angle between the netting and the incoming flow (Bi et al. [25]; Zhao et al. [26]), and the biofouling on netting (Bi et al. [27]; Gansel et al. [28]) but unlikely as the nets were cleaned.

3.2.2.1. Data obtained from the turbulence profiler.
All vertical profiling was performed upstream of the farm (labeled "Upstream"), at the leeward side of the cage (labeled "Lee of Cage2") and the downstream of the cage (labeled "Downstream") (Fig. 11). In front of and downstream of the cage, the profiles were collected from the freely moving boat that drifted according to the wind and current flow at the surface. For this reason, it was not always possible to perform moving profiling following a straight line with the directions passing through the cage. At the leeward side, care was taken that the turbulence profiler did not impact the net of the cage. In Phase A, profiling was performed over two days (P1: 09 August 2018; P2: 15 August 2018). In Phase B, profiling was performed in one day (P3: 11 October 2018). All data are presented as follows (Fig. 11): Pd_D denotes profiles on downstream of the farm; Pd_U denotes profiles upstream of the farm in relation to the flow direction (NE to SW), d = 1,2,3 (three days)

In this study, we aimed to determine the alterations in turbulence dissipation and temperature in relation to the structure of the fish cage. Methods for the estimation of the turbulence dissipation rate $\mathcal{E}$ (Moum et al.[29]; Lueck [17]) and the corresponding results are presented in the following paragraphs.

Shear probes are used to measure small-scale turbulence in different environments. Since they were introduced (Osborn [30]), they have been mounted on various platforms, such as vertical profilers (e.g., the present study), mooring lines, and gliders (Fer et al. [31]). Because of their low noise levels and high sampling rates, these probes are used to gather precise high-resolution measurements. Shear probes sense velocity fluctuations cross-stream to their direction of travel, such as x_3 along the vertical direction in the present study. The two shear probes (S_1 and S_2) were mounted orthogonal to each other in order to measure the vertical gradient of each component of horizontal flow $\partial u_1/\partial x_3$ and $\partial u_2/\partial x_3$, where u_1, u_2 and u_3 are the velocity components in an orthogonal coordinate system given by x_1, x_2 and x_3. $\mathcal{E}$ is the primary turbulence parameter that is computed from these shear probes. It
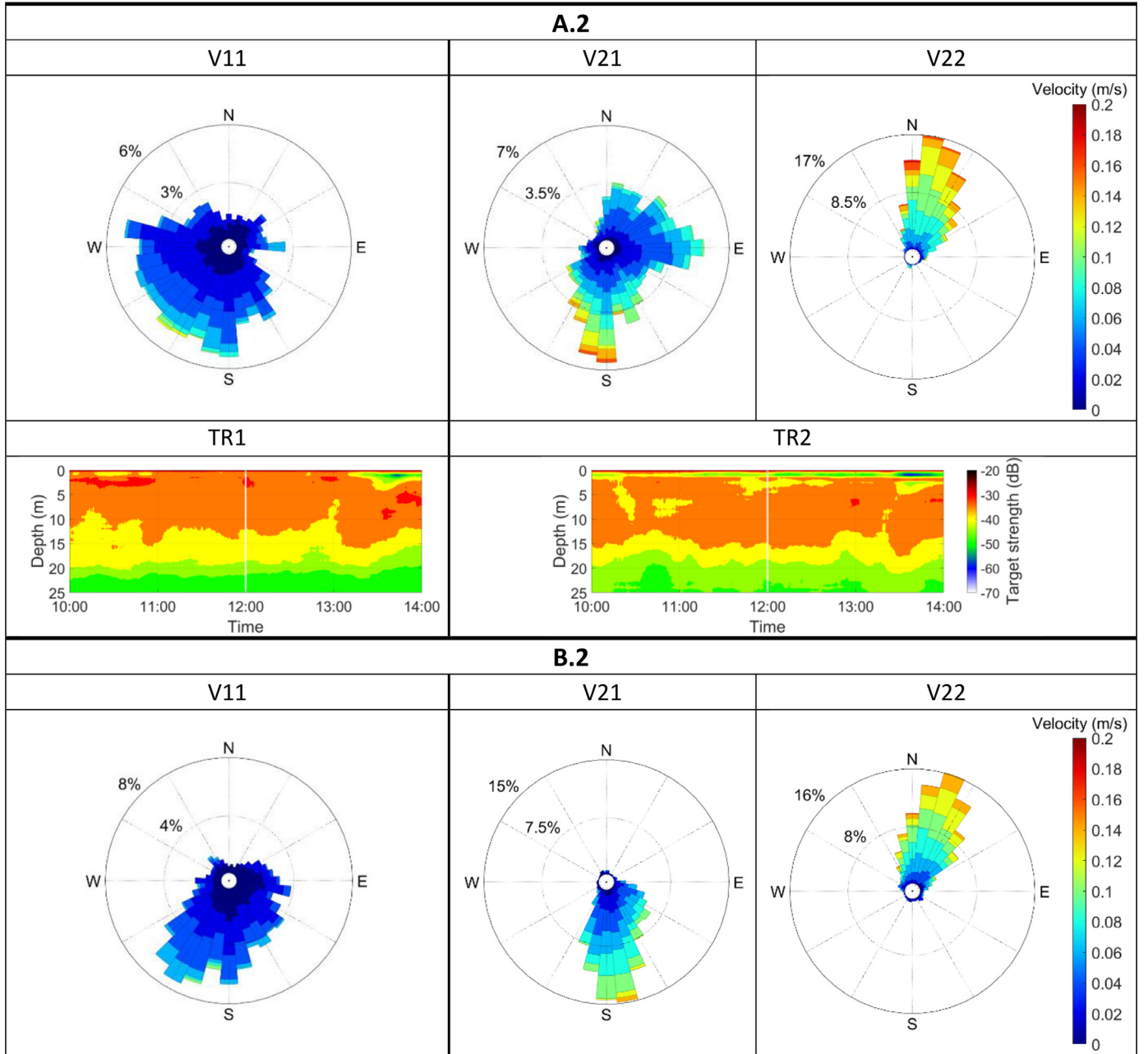
Fig. 4. Velocity magnitude (Horizontal component) and current rose, of the velocity inside the cage at different depths and locations (V11, V21, V22) for A.2 and B.2. In Phase A (with stocked cage), the corresponding signals of the echosounders at the same locations are added.

describes the transfer of energy from the mean flow to the turbulent flow, and its value is related to the magnitude of the turbulent velocity fluctuations. The turbulence parameter ε is estimated by measuring the velocity shear using the shear probe and integrating the shear spectrum obtained during each profile. Regardless of the travel direction of the sensor, the rate of dissipation ε of TKE in isotropic turbulence is given by the following equation:

$$\varepsilon = \frac{15}{2}\nu \overline{\left(\frac{\partial u_i}{\partial x_j}\right)^2} = \frac{15}{2}\nu \int_0^\infty \psi(k)dk, \tag{3}$$

where ν is the kinematic viscosity of water, the overbar denotes a time-averaged quantity, and ψ is the spectrum of the shear $(\frac{\partial u_i}{\partial x_j})$. An empirical spectrum of velocity fluctuations was derived by Nasmyth [32] and formally published by Oakey [33] as a tabulated shear spectrum, which is referred to as the Nasmyth spectrum. This spectrum is used to pad the

spectra from the measurements, which give an estimation of the dissipation ε (Macoun and Lueck [34]). All the raw data are first de-spiked to remove wrong transient records that are the most likely to be linked to interactions with biological organisms. Only the data with the pitch of the falling micro CTD lower than 1 deg during all the profiles are considered. In the next level of post-processing, profiles are not considered in which the two dissipation rates do not agree with the two shear probes (S_1 and S_2). Finally, another misfit criterion is the quality of the spectrum. To discard spectra that deviated unreasonably from the shape of the Nasmyth empirical spectrum, we used the mean absolute deviation (MAD) defined as follows, which is estimated for n spectral observations:

$$MAD = \frac{1}{n} \sum_{i=1}^{n} \left| \frac{\overline{\psi_{\partial u_i/\partial x_j}}}{\psi_M} - \frac{\overline{\psi_{\partial u_i/\partial x_j}}}{\psi_M} \right|, \tag{4}$$
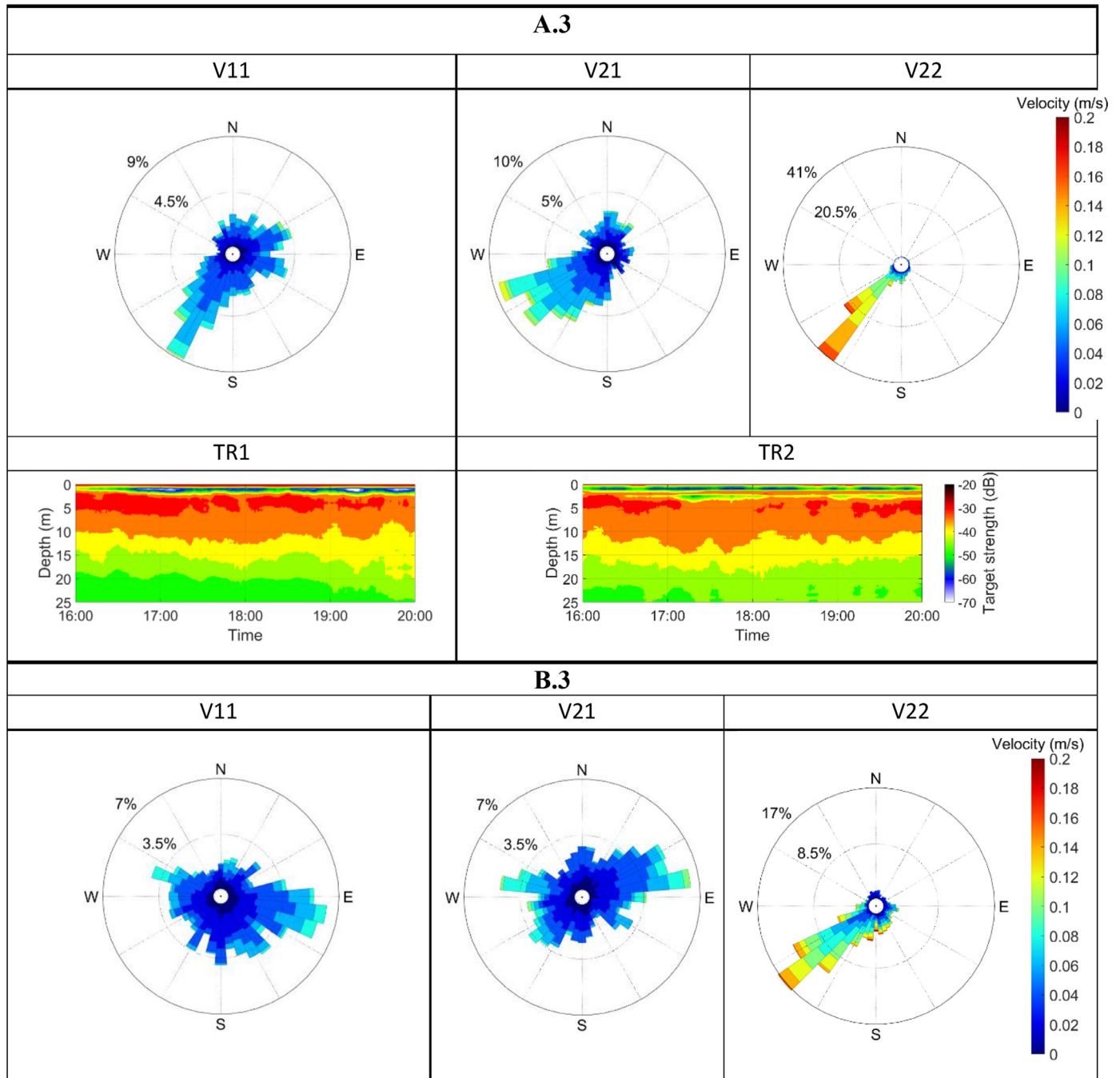
Fig. 5. Velocity magnitude (Horizontal component) and current rose, of the velocity inside the cage at different depths and locations (V11, V21, V22) for A.3 and B.3. In Phase A (with stocked cage), the corresponding signals of the echosounders at the same locations are added.

where ψ_M is a theoretical formulation of the Nasmyth empirical spectrum (Lueck [17]): $\psi_M = \frac{8.05\, x^{1/3}}{1+(20.6\, x)^{3.715}}$, where $x = k\eta = k(\nu^3/\epsilon)^{1/4}$ and k the wavenumber

A data segment was rejected if the MAD is greater than $2\sqrt{2/d}$ where d is the degree of freedom (DOF) of the measured spectrum. This rejection limit is twice that of the perfect fit as computed by Ruddick et al. [35]. In this study, all data with a MAD value lower than 0.5 were not considered.

The ODAS MATLAB Library V4.3 (Rockland) was used for the processing of the raw data obtained from the turbulence profilers. As explained previously, the shear spectrum was generated for each depth bin and then compared with a pseudo shear spectrum that was generated from the accelerometer data. Three parameters were used to post-

process the data using the ODAS Library: 1) FFT_length = 1 s, because the current dissipation rates are mainly in the 10^{-7} to 10^{-6} W/kg range, which means that in the Nasmyth spectrum, the peak will occur at a high frequency/wavenumber (Lueck [17]) (FFT: Fast Fourier Transform); 2) Diss_length = 4 controls the number of spectra from the "FFT_length" segments that are averaged, taking into account the falling speed of the MicroCTD ($\sim$0.75 m/s), allowing the 3 m-depth bins to be analyzed separately; 3) Overlap = 2, which controls the number of spectra from the "FFT_length" segments that are averaged.

In summary, each profile was split into segments of 2048 samples (4 s) that were overlapped by 50%. The profiles of the turbulence dissipation rate ε are presented in Fig. 12, Fig. 13, and Fig. 14. The corresponding temperature profiles are presented in Fig. 15, Fig. 16, and Fig. 17. These data were collected in the measurements taken on three
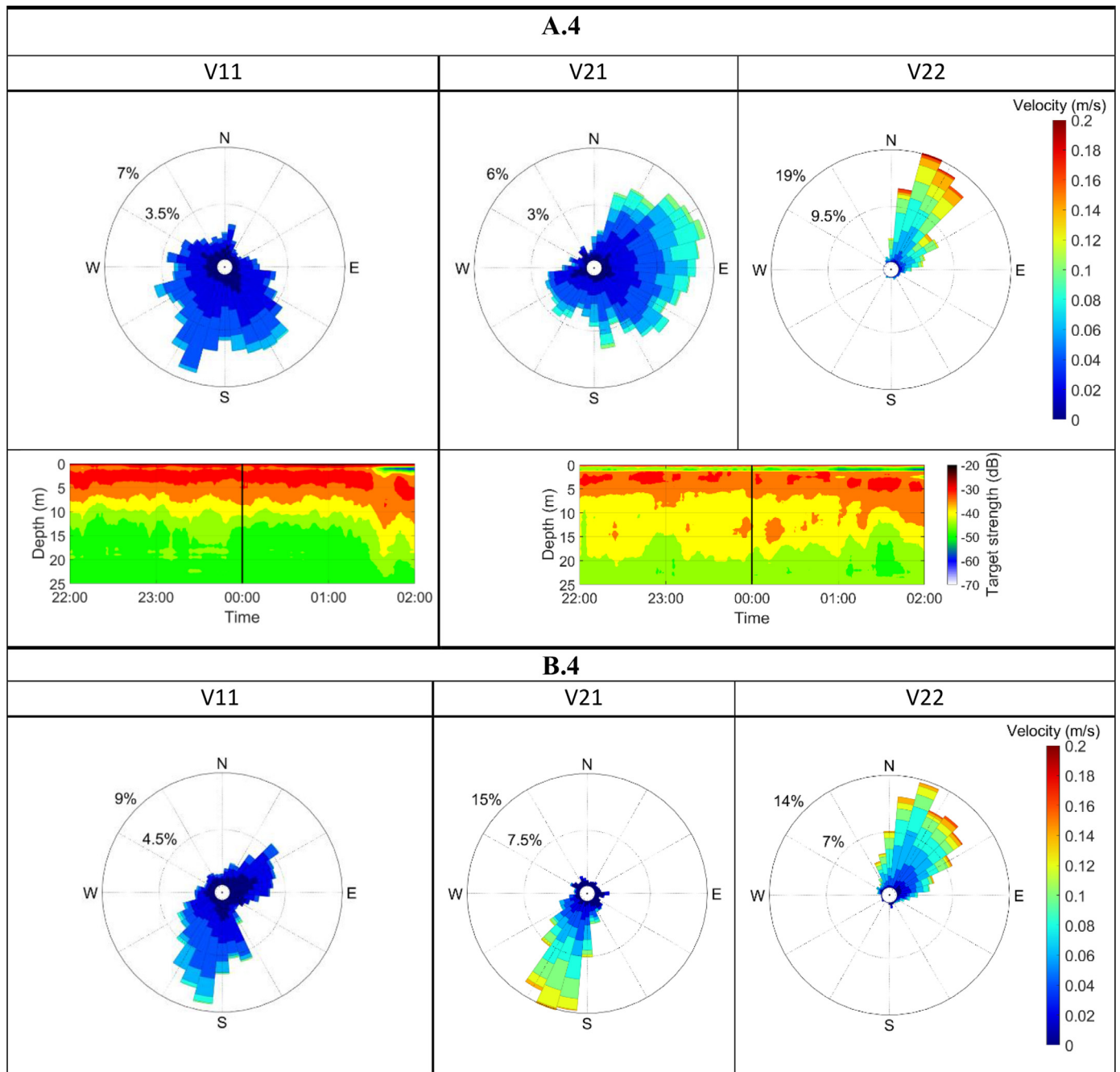
Fig. 6. Velocity magnitude (Horizontal component) and current rose, of the velocity inside the cage at different depths and locations (V11, V21, V22) for A.4 and B.4. In Phase A (with stocked cage), the corresponding signals of the echosounders at the same locations are added.

Table 2
Velocity reduction on the wake of cage2, calculated with the data from the moving ADCP and compared with Løland [20] formulation for phase B (without fish).

Depth	u_w	U_0	u_w/U_0	r (Løland)
5 m (skirt)	0.23	0.09	0.39	
10 m (skirt)	0.22	0.10	0.47	
12 m (net cylinder)	0.21	0.12	0.56	0.71
14 m (net-cylinder)	0.20	0.13	0.66	0.71
20 m (net-cone)	0.18	0.17	0.93	

different days (d = 1, 2, and 3), and they were split into three categories (Fig. 11) downstream (Pd_D, d = 1,2,3), at the cage, and

upstream (Pd_U, d = 1,2,3) in a northeast incoming flow direction. Both downstream and upstream profiles were performed when the boat was drifting freely (moving either by the surface current or/and by a light surface wind). The profile at the cage was performed in exactly the same position as in the lee of the cage. For the measurements downstream and upstream, the MicroCTD was reeled up far before it reached the bottom because of the uncertainties of the bottom topography when the boat was drifting freely. Hence, the measurement depths were shorter than those in the lee of the cage. All these profiles were performed during well-establish flow and at low time intervals between series.

Although it was not possible to perform the same profiling lines upstream and downstream in all series during the three days of measurements, a clear pattern was observed in the dissipation rate (ε)
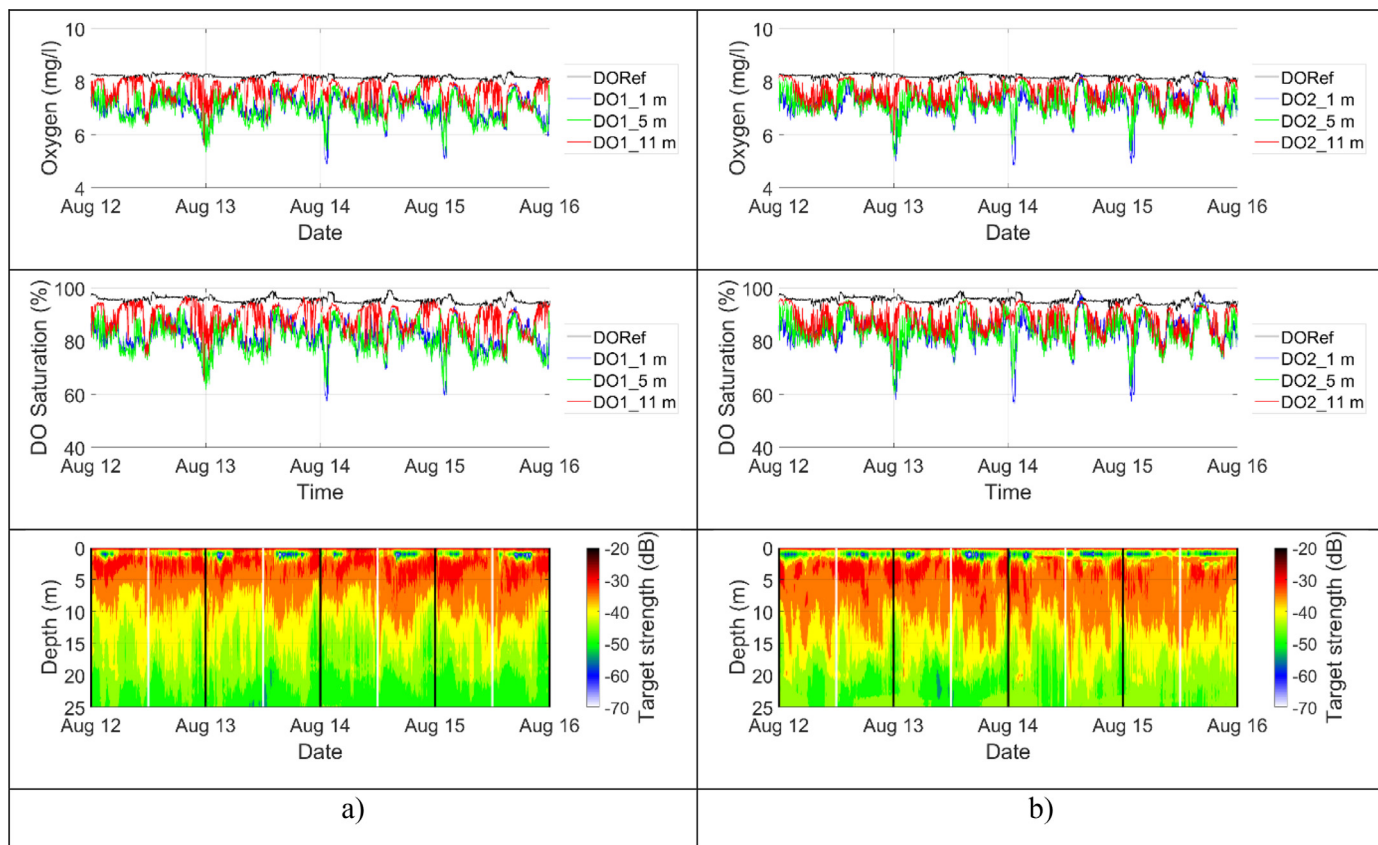
Fig. 7. DO variations inside the cage (upper cells) with corresponding echosounder signals: (a) 18 m from the center; b) at the center. Echosounders (white vertical line, midday; black vertical line, midnight). DO color code (blue 1 m, green 5 m, red 11 m, black: reference location). All data shown are from Phase A. (For interpretation of the references to color in this figure legend, the reader is referred to the web version of this article.)
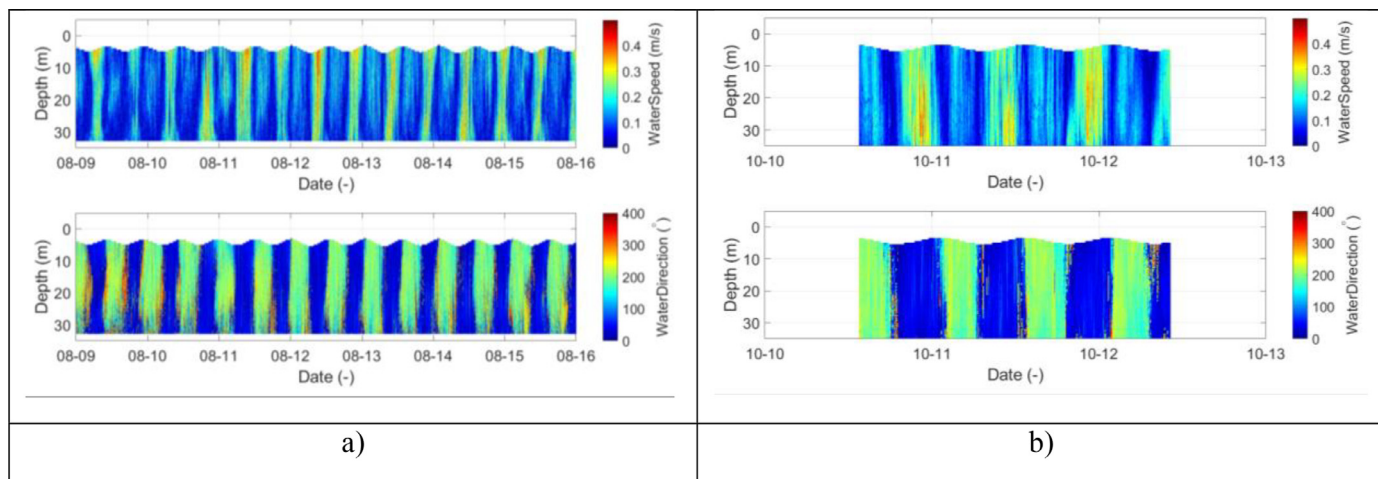

Fig. 8. Velocity profile and direction of ADCP1 during the two phases (a) A and (b) B.

profiles. The magnitudes of dissipation rate measured upstream and downstream were in the same order during each day of measurement, while the magnitudes of the *dissipation rate* measured in the lee of the cage was about one order higher along the depth of the cylindrical part of the cage (15 m). Even higher values were found along the skirt depth, which was also shown in lab scale measurements and simulations with porous and solid cylinders (Gansel et al. [36]; Shim et al. [37]).

The *dissipation values* measured in the lee of the cage showed a decrease with water depth, and reached the dissipation values measured at the corresponding depths in the upstream and downstream locations when approaching the bottom of the cage. However, this

decrease was not constant and large variations were measured at 20–26 m on day 1 and at 17–22 m on day 2, the variations on day 3 were not as obvious as on day 1 and day 2.

A possible explanation is that from depths of 15 m to 27 m, the cage had a conical shape, which affected the flow differently from the vertical nets in the upper part with the same porosity. The orientation of the nets in the cone part was around 65 deg in the vertical direction. Patursson et al. [38] showed that a net panel with a 60-deg angle of attack reduced the incoming flow 50% less than a panel perpendicular to the flow direction as in the upper part of the cage, which will lead to a complex interaction zone in the vicinity of the cage. This complexity
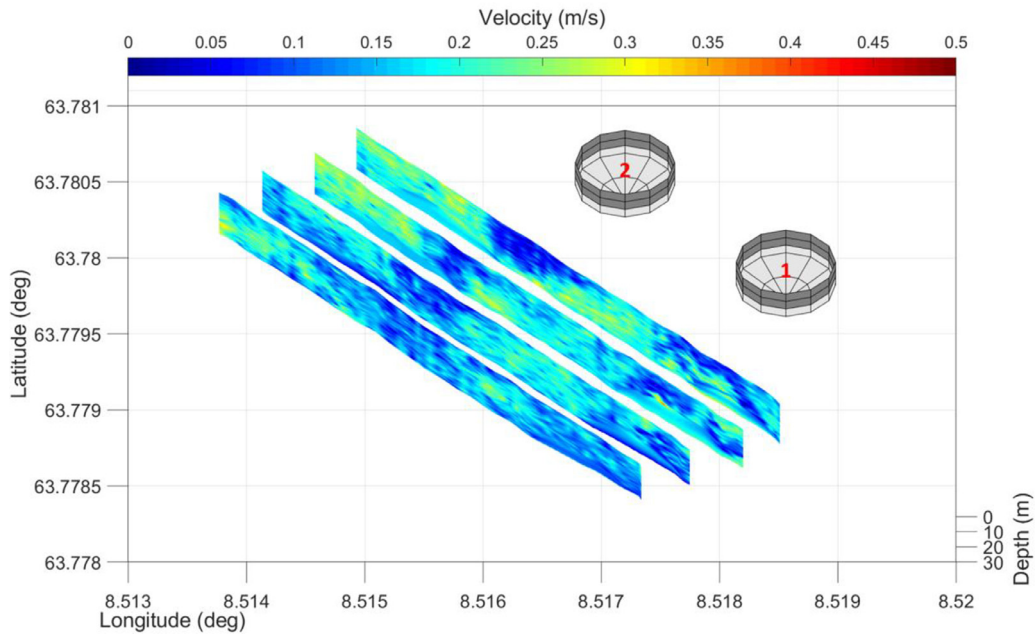
Fig. 9. Visualization of the velocity field in vertical plans from the transects performed in the wake of the two cages during Phase B (without fish).
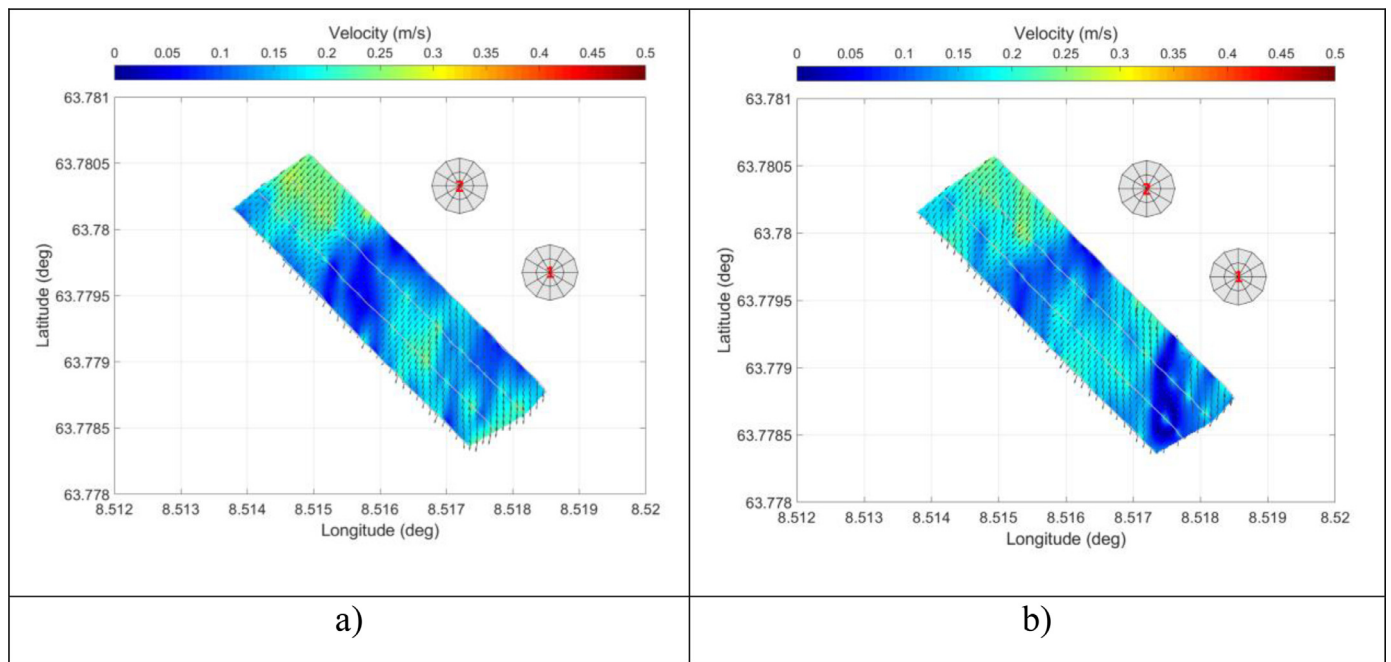

Fig. 10. Visualization of the velocity field in horizontal planes at different depths during phase B: (a) 6 m; (b)12 m from interpolation of the vertical transects performed in the wake of two cages.

is enhanced if the incoming flow is not completely two-dimensional (with mainly the horizontal components), and if there is a temperature gradient in the water column, which occurred during these measurements. It should also be noted that these large variations in the *dissipation* profiles recorded on day 1 and day 2 under the cylindrical part of the cage could not be related to the biomass as only low fish distribution were detected in this area (Fig. 7).

The assumptions that three-dimensional complex flow structures were generated in the conical part of the cage and interacted with the lower depths of the cylindrical part were supported by the results of the temperature profiles derived using the fast Micro-temperature (FP07) sensor integrated in the MicroCTD. The data taken from the temperature sensors during the same profiles are plotted in Fig. 15, Fig. 16, and

Fig. 17. On day 1 and day 2, a temperature gradient of 0.5–0.8° occurred in the first 30 m of the water column. The upstream and downstream profiles showed smooth decreases from the water surface, whereas the profiles taken in the lee of the cage showed large decreases at 21 m–26 m on day 1 and at 17 m–24 m on day 2, which implied that the water at these depths was mixed with the cold layer of water below the cage. The difference in the heights of the mixing region could be related to the higher incoming current velocity on day 2. In contrast, on day 3, no temperature gradient occurred at the same depths, and therefore no mixing was observed.
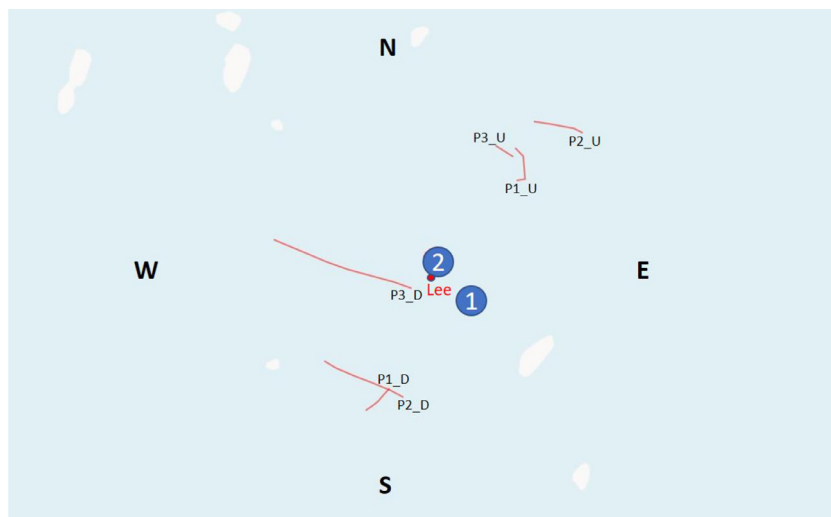
Fig. 11. Schematic view of the MicroCTD deployment profiling lines around cage 2.
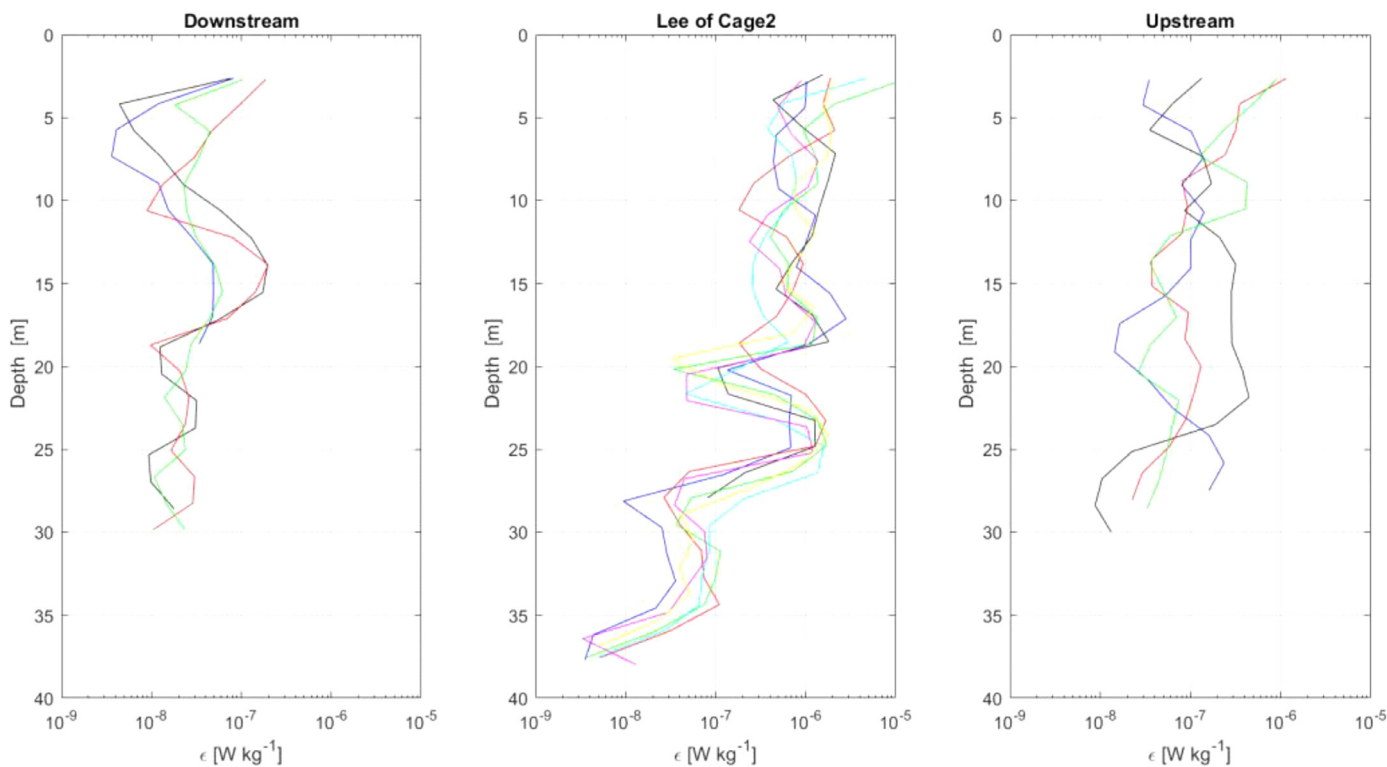

Fig. 12. Dissipation profiles based on several casts downstream of the farm, in the lee of cage 2, and upstream of the farm on day 1, d = 1: 09 August 2018. For the upstream and downstream profiles, the MicroCTD was reeled up much before it reached the sea bottom (35–40 m).

4. Conclusion

In this study, the measurement results showed the association of three-dimensional measurements of the current flow field, turbulence in the vicinity of the commercial salmon cage, shielded with 10 m depth skirt from the surface, with flow velocity, dissolved oxygen and fish distribution measurements inside the cage. These results contribute new insights into flow modifications that are caused by sea cages. The flow measurements inside the cage showed that the large swimming salmon did not alter the flow pattern noticeably except reducing the flow velocity: no significant vertical and radial flows were measured in the shielded volume where low flow velocity occurred. The main flow pattern inside the cage with fish was quite similar to that in the cage without fish. Lowest oxygen level was registered inside the shielded

cage volume during nighttime when fish gathered mainly at the surface.

The flow reduction recorded downstream of the cage extended to at least three cage diameters, and a clear effect of the skirt was found within the first two cage diameters. The turbulence profiles performed upstream, downstream, and in the lee of the cage showed strong modifications of the turbulence levels across a range of different background flow conditions. The turbulence levels in the lee side of the cage, in the upper 20 m of the water column, showed highly elevated rates of turbulence up to one order higher than those observed several hundred meters upstream and downstream of the cage. Higher turbulence levels were also repeatedly measured in the upper 10 m of the water column compared to those measured, below 10 m, in the lee of the cage, which was due to the skirt around the cage. No noticeable effects of the swimming salmon were observed, and similar levels of
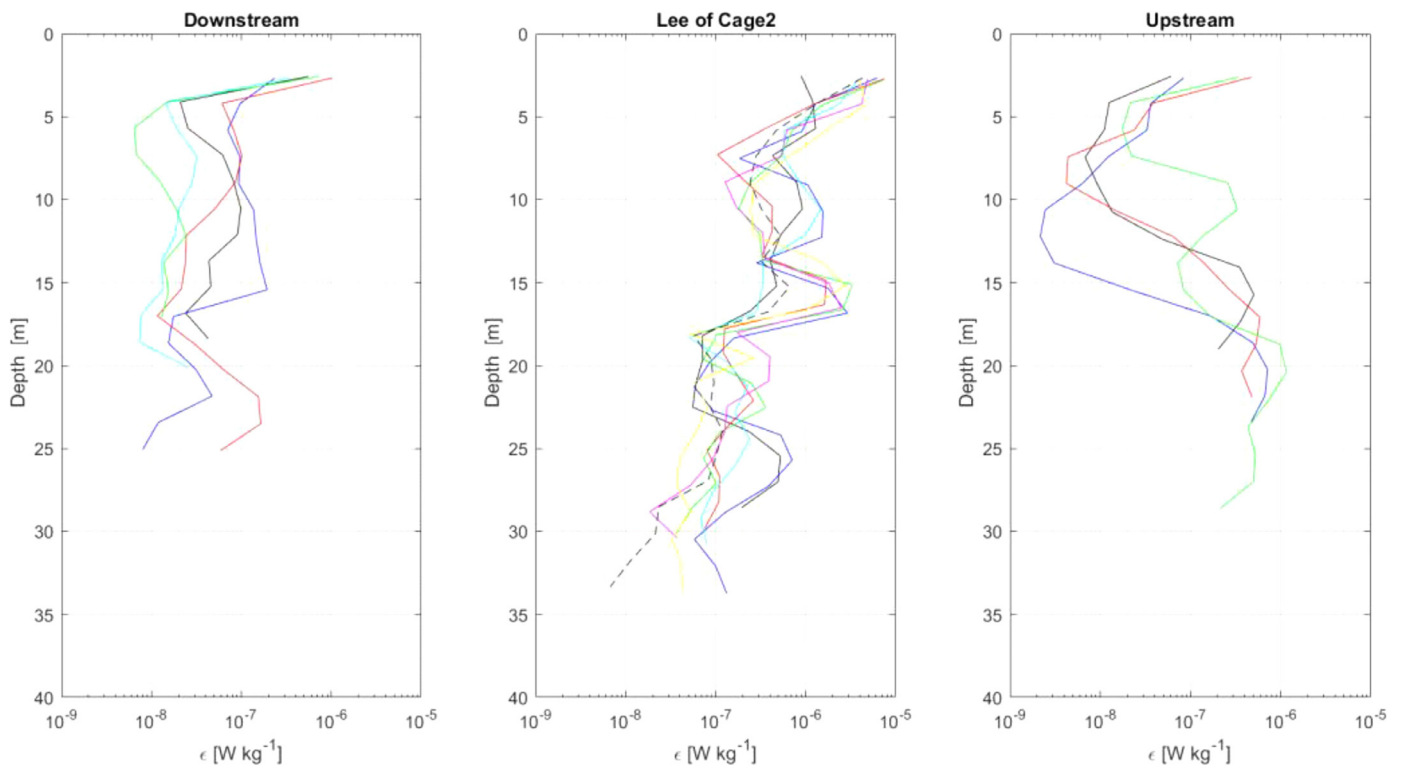
Fig. 13. Dissipation profiles based on several casts downstream of the farm, in the lee of cage 2, and upstream of the farm on day 2, $d = 2$: 15 August 2018. For the upstream and downstream profiles, the MicroCTD was reeled up much before it reached the sea bottom (35–40 m).
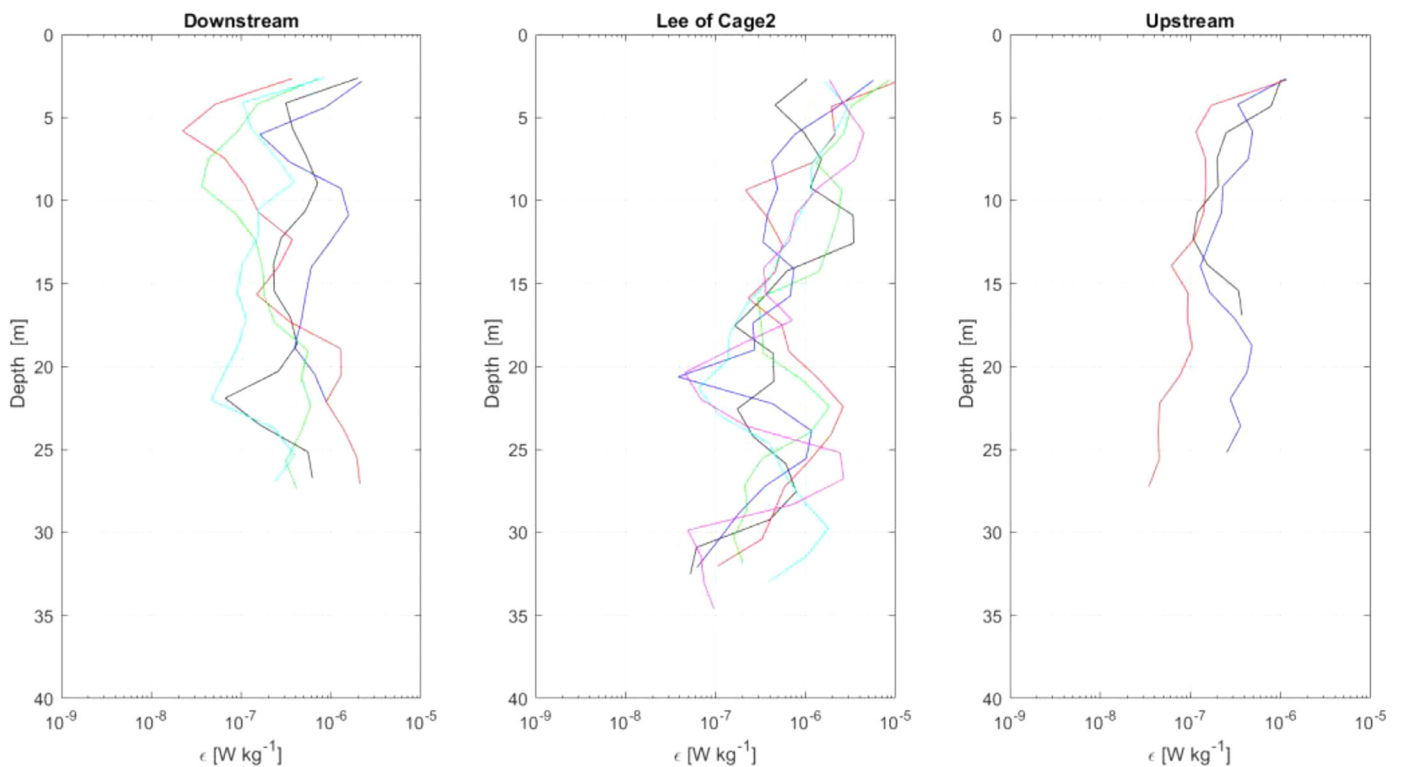

Fig. 14. Dissipation profiles based on several casts downstream of the farm, in the lee of cage 2, and upstream of the farm on day 3, $d = 3$: 11 October 2018. For the upstream and downstream profiles, the MicroCTD was reeled up much before it reached the sea bottom (35–40 m).

turbulence were recorded for the cage with and without fish. These results indicate that the aquaculture sea cages significantly altered the three-dimensional flow field, the intensity and distribution of the turbulence levels, and so the water mixing in the lee of the cage. This combination of strong flow reductions and high turbulence, on the wake of the cage, will have different effects on the spreading of particles with distinct densities and also micro-organisms like pathogens and zooplanktons.
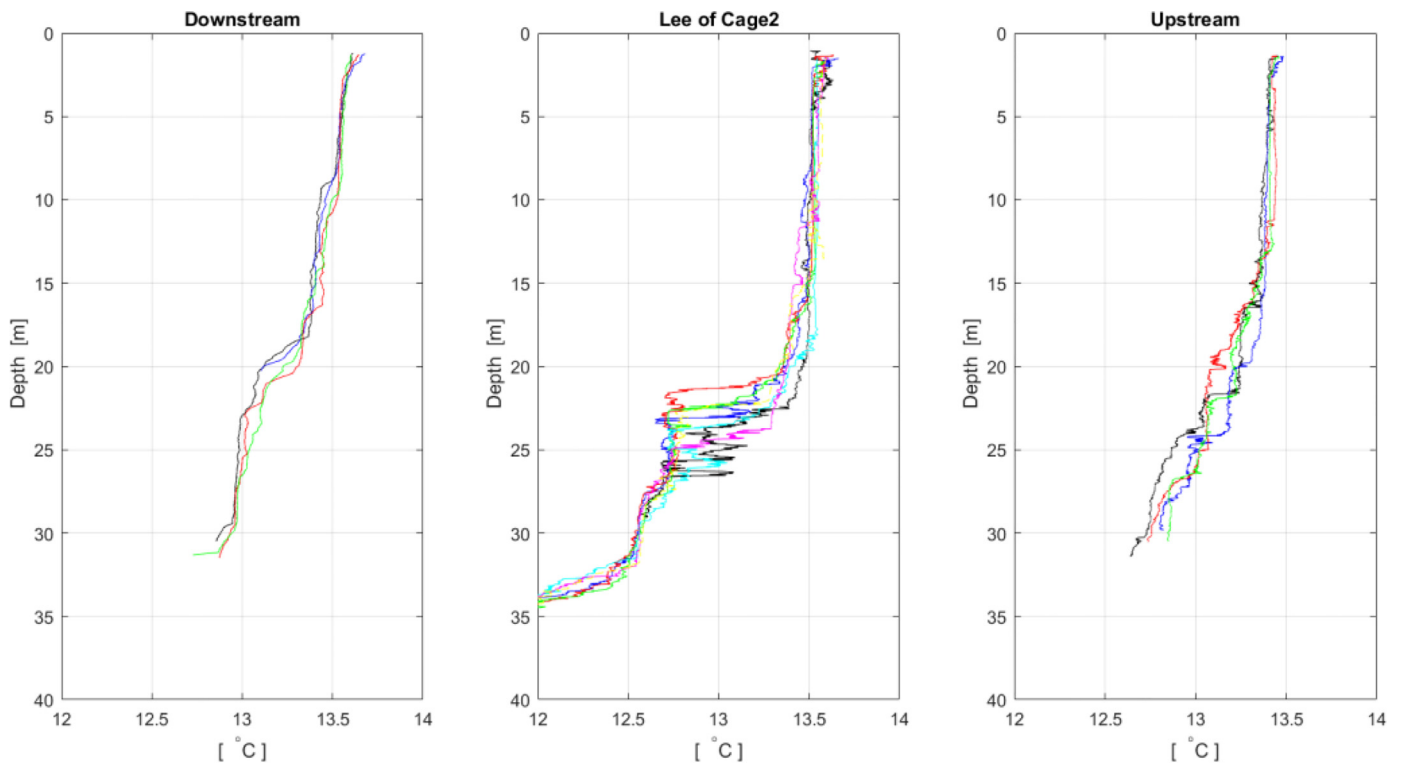
Fig. 15. Temperature profiles from several casts, downstream the farm, in the lee of cage 2, and upstream of the farm on 09 August 2018.
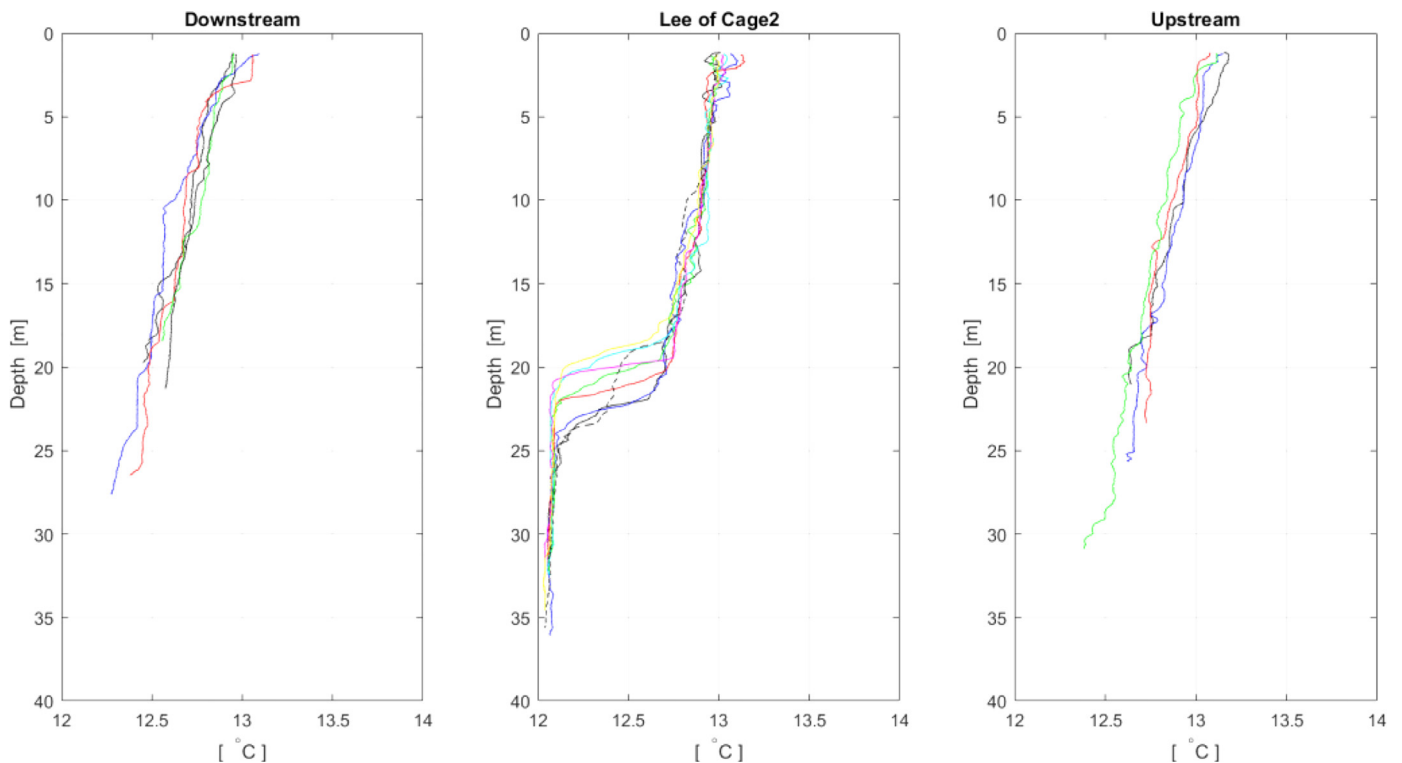

Fig. 16. Temperature profiles based on several casts on the wake of the farm, in the lee of cage 2, and in front of the farm on 15 August 2018.

CRediT author statement

Pascal KLEBERT: Planing, Supervision and performing the measurement, Post processing of the data, Writing- Original draft, Methodology.

Biao Su: post- processing of data, Writing- Reviewing and Editing.

Declaration of Competing Interest

The authors declare that they have no known competing financial interests or personal relationships that could have appeared to influence the work reported in this paper.
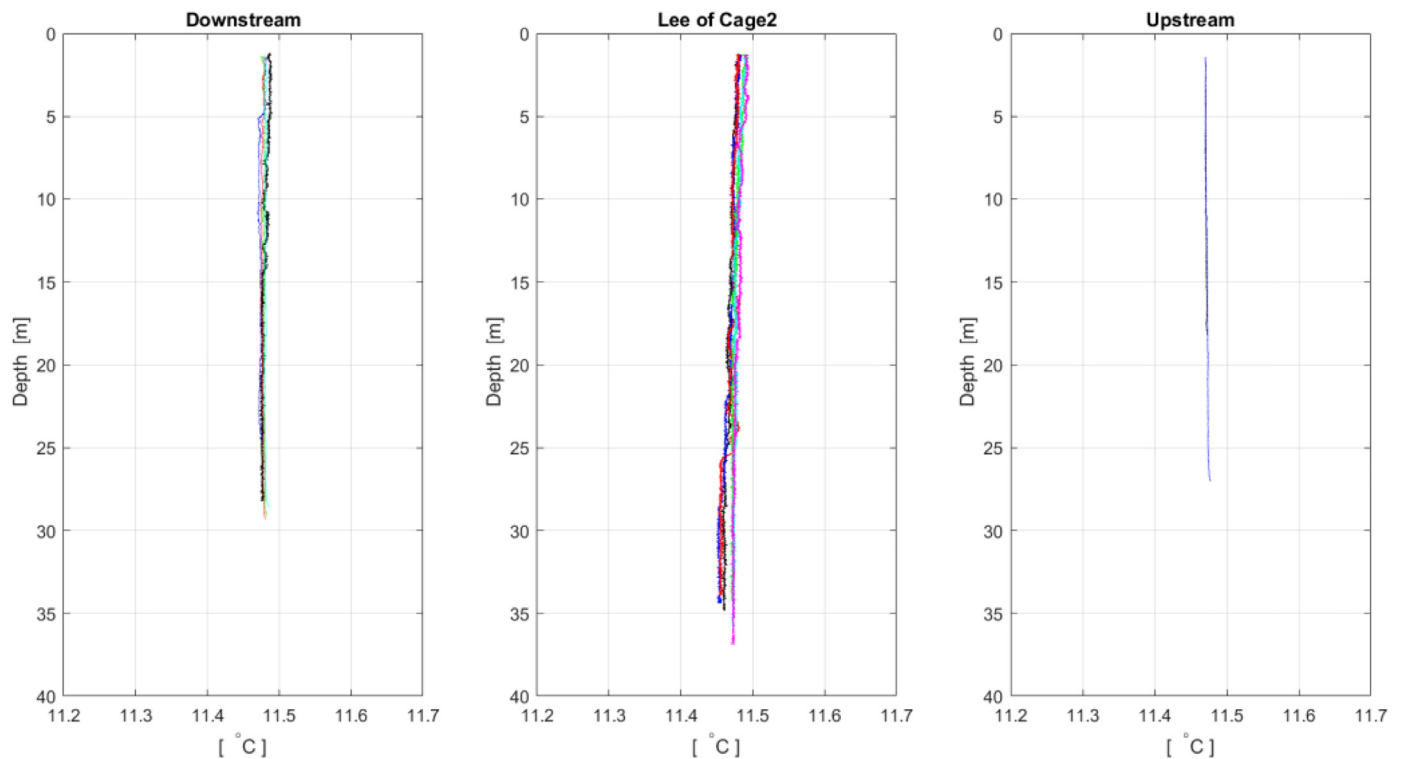
Fig. 17. Temperature profiles based on several casts in the wake of the farm, in the lee of cage 2, and in front of the farm on 11 October 2018.

Acknowledgements

References

[1] FAO, The State of World Fisheries and Aquaculture 2018 - Meeting the Sustainable Development Goals, 2018 Rome.

[2] P. Klebert, H.W. Rasmussen, Ø Patursson, Three-Dimensional Flow Field Visualization in the Wake of a Group of Fish Farming Sea Cages, World Aquaculture Society (WAS), Adelaide, Australia, 2014.

[3] P. Klebert, Ø. Patursson, P.C. Endresen, P. Rundtop, J. Birkevold, H.W. Rasmussen, Three-dimensional deformation of a large sea cage in high currents: experiments and simulation, J. Ocean Eng. (2015) 511–520.

[4] C.W. Bi, Y.P. Zhao, G.H. Dong, Y.N. Zheng, F.K. Gui, A numerical analysis on the hydrodynamic characteristics of net cages using coupled fluid–structure interaction model, Aquacult. Eng. 59 (2014) 1–12.

[5] T. Kim, J. Lee, D.W. Fredriksson, J. DeCew, A. Drach, K. Moon, Engineering analysis of a submersible abalone aquaculture cage system for deployment in exposed marine environments, Aquacult. Eng. 63 (2014) 72–88.

[6] Y. Zhao, C. Bi, C. Chen, Y. Li, G. Dong, Experimental study on flow velocity and mooring loads for multiple net cages in steady current, Aquacult. Eng. 67 (2015) 24–31, https://doi.org/10.1016/j.aquaeng.2015.05.005.

[7] H.W. Rasmussen, Ø. Patursson, K. Simonsen, Visualisation of the wake behind fish farming sea cages, Aquacult. Eng. 64 (2014) 25–31.

[8] P. Klebert, P. Lader, L. Gansel, F. Oppedal, Hydrodynamic interactions on net panel and aquaculture fish cages: a review, Ocean Eng. 58 (2012) 260–274.

[9] L.C. Gansel, T.A. McClimans, D. Myrhaug, The effects of fish cages on ambient currents, J. Offshore Mech. Arct. Eng. 134 (1) (2012) 011303.

[10] D. Johansson, F. Laursen, A. Fernö, J.E. Fosseidengen, P. Klebert, L.H. Stien, T. Vågseth, F. Oppedal, The interaction between water currents and salmon swimming behaviour in sea cages, PLoS ONE 9 (5) (2014) e97635.

[11] P. Klebert, L. Arneborg, Flow Hydrodynamics and Oxygen Level Distribution Around and Within Large Fish Cages: Measurements, World Aquaculture Society, Adelaide, South Australia, 2014.

[12] D. Plew, P. Klebert, T. Rosten, S. Aspaas, J. Birkevold, Flow and turbulence modifications by different densities of fish in a circular tank, J. Hydraul. Res. (2015), https://doi.org/10.1080/00221686.2015.1029016.

[13] Ø. Skagseth, K. Drinkwater, E. Terrile, Wind and buoyancy induced transport of the Norwegian coastal current in the Barents Sea, J. Geophys. Res. 116 (2011) C08007, https://doi.org/10.1029/2011JC006996.

[14] R. Sætre, The Norwegian Coastal Current: Oceanography and Climate, The Institute of Marine Research/Academic Press, Bergen/Tapir, 2007.

[15] K. Frank, L. Gansel, A. Lien, J. Birkevold, Effects of a shielding skirt for prevention of sea lice on the flow past stocked salmon fish cages, J. Offshore Mech. Arct. Eng. (2014) 137, https://doi.org/10.1115/1.4028260.

[16] F. Wolk, H. Yamazaki, L. Seuront, R.G. Lueck, A new freefall profiler for measuring bio-physical microstructure, J. Atmos. Ocean. Tech. 19 (2002) 780–793.

[17] R. Lueck, Calculating the Rate of Dissipation of Turbulent Kinetic Energy, Rockland Scientific International, Victoria, Canada, 2016 RSI technical note 028.

[18] D.G. Goring, V.I. Nikora, Despiking acoustic doppler velocimeter data, J. Hydraul. Eng. 128 (1) (2002) 117–126.

[19] A.M. Lien, L.H. Stien, R. Grøntvedt, K. Frank, Permanent Skjørt for Redusering av Luspåslag på laks, (2015) Sluttrapport, FHF-prosjekt 900711. SINTEF Rapport.

[20] F. Oppedal, T. Dempster, L.H. Stien, Environmental drivers of Atlantic salmon behaviour in sea-cages: a review, Aquaculture 311 (2011) 1–18.

[21] D. Solstorm, T. Oldham, F. Solstorm, P. Klebert, L.H. Stien, T. Vågseth, F. Oppedal, Dissolved oxygen variability in a commercial sea-cage exposes farmed Atlantic salmon to growth limiting conditions, Aquaculture 486 (2018) 122–129.

[22] Hajovsky R., Filipova B., Pies M., Ozana, S., Using Matlab for thermal processes modeling and prediction at mining dumps, in: Proceedings of the 12th International Conference on Control, Automation and Systems (ICCAS). Jeju Island, Korea, October 17–21(2012) pp. 584–587.

[23] G. Løland, Current forces on, and water flow through and around, floating fish farms, Aquacult. Int. 1 (1993) 72–89.

[24] Y.P. Zhao, Y.C. Li, G.H. Dong, F.K. Gui, B. Teng, Numerical simulation of the effects of structure size ratio and mesh type on three-dimensional deformation of the fishing-net gravity cage in current, Aquacult. Eng. 36 (2007) 285–301.

[25] C.W. Bi, Y. Zhao, G. Dong, T.J. Xu, F.K. Gui, Experimental investigation of the reduction in flow velocity downstream from a fishing net, Aquacult. Eng. 57 (2013) 71–81.

[26] Y.P. Zhao, C.W. Bi, G.H. Dong, Numerical simulation of the flow around fishing plane nets using the porous media model, Ocean Eng. 62 (2013) 25–37.

[27] C.W. Bi, Y.P. Zhao, G.H. Dong, Z.M. Wu, Y. Zhang, T.J. Xu, Drag on and flow through the hydroid-fouled nets in currents, Ocean Eng. 161 (2018) 195–204.

[28] L.C. Gansel, D.R. Plew, P.C. Endresen, A.I. Olsen, E. Misimi, J. Guenther, Ø Jensen, Drag of clean and fouled net panels–measurements and parameterization of fouling, PLoS ONE 10 (7) (2015) e0131051.

[29] J.N. Moum, M.C. Gregg, R.C. Lien, M.E. Carr, Comparison of turbulence kinetic energy dissipation rate estimates from two ocean microstructure profilers, J. Atmos. Oceanic Technol. 12 (1995) 346–366.

[30] T.R. Osborn, Vertical profiling of velocity micro-structure, J. Phys. Oceanogr. 4

(1974) 109–115, https://doi.org/10.1175/1520-0485.

[31] I. Fer, M.B. Paskyabi, Autonomous ocean turbulence measurements using shear probes on a moored instrument, J. Atmos. Oceanic Technol 31 (2014) 474–490.

[32] P.W. Nasmyth, Oceanic Turbulence, University of British Columbia, 1970.

[33] N.S. Oakey, Determination of the rate of dissipation of turbulent energy from simultaneous temperature and velocity shear microstructure measurements, J. Phys. Oceanogr. 12 (1982) 256–271.

[34] P. Macoun, R. Lueck, Modeling the spatial response of the airfoil shear probe using different sized probes, J. Atmos. Ocean. Technol. 21 (2004) 284–297.

[35] B. Ruddick, A. Anis, K Thompson, Maximum likelihood spectral fitting: the Batchelor spectrum, J. Atmos. Oceanic Technol. 17 (1) (2000) 1541–1555.

[36] L.C. Gansel, T.A. McClimans, D. Myrhaug, The effects of fish cages on ambient currents (2012), J. Offshore Mech. Arct. Eng. 134 (1) (2012) 011303.

[37] Shim, K., Klebert, P., Fredheim, A., Numerical investigation of the flow through and around a net cage. ASME 2009 28th. International Conference on Ocean, Offshore and Arctic Engineering, (2009) pp. 581–587.

[38] Ø. Patursson, M.R. Swift, I. Tsukrov, K. Simonsen, K. Baldwin, D. Fredriksson, C. Barbaros, Development of a porous media model with application to flow through and around a net panel, Ocean Eng. 37 (2) (2010) 314–324.